



Cite this: *Phys. Chem. Chem. Phys.*,  
2021, **23**, 11917

## A theoretical study of wrinkle propagation in graphene with flower-like grain boundaries<sup>†</sup>

Zihui Zhao,<sup>‡ab</sup> Yafei Wang,<sup>‡ab</sup> and Changguo Wang <sup>ID</sup> <sup>\*ab</sup>

This study investigated dynamic surface wrinkle propagation across a series of flower-like rotational grain boundaries (GBs) in graphene using theoretical solutions and atomistic simulations. It was found that there was significantly less out-of-plane displacement of dynamic wrinkles when curvature of rotational GBs was reduced, which can be explained by a defect shielding effect of flower-like GBs. Potential energy evolved via different modes for pristine graphene and graphene with various GBs. With external excitation, the distinctly different patterns of wrinkle propagation in graphene with various GBs demonstrated how dynamic wrinkling can reveal defects. These results can provide a theoretical basis for guiding the design and implementation of graphene-based nano-mechanical devices such as protectors and detectors.

Received 22nd March 2021,  
Accepted 6th May 2021

DOI: 10.1039/d1cp01254a

rsc.li/pccp

### 1. Introduction

The ability to understand the underlying physics of graphene, and its potential applications in novel devices, is a topic of particular interest.<sup>1–5</sup> Graphene monolayers have exceptional mechanical properties, including spontaneous and controlled wrinkling,<sup>6–8</sup> which are expected to strongly influence their electronic properties by introducing spatially varying potentials<sup>9,10</sup> or gauge fields,<sup>11–13</sup> as reported for periodic wrinkles with wavelengths of 2.4–3.0 nm and amplitudes of 0.02–0.05 nm.<sup>14–16</sup> This allows electromechanical characterization of graphene strain-based resonators with fundamental frequencies of megahertz to terahertz.<sup>5,6,17,18</sup> To that end, it is essential to determine the mechanical properties of strain-based graphene in the nanometer range, especially their dynamic nature, and time dependence of graphene's elastic behavior.<sup>19–25</sup>

Generally speaking, the last decade has witnessed rapid achievements in surface topographical modulation of strain-based graphene,<sup>8,26,27</sup> and recent experiments have inspired several strategies for developing controlled wrinkles in graphene monolayers.<sup>18,28–30</sup> One strategy uses the finite size effects of substrates, including lattice mismatch and substrate corrugation and curvature,<sup>29,31–36</sup> to produce spatially

nonuniform strain in graphene. When monolayer graphene is grown on single-crystal metal surfaces<sup>19,37,38</sup> (such as Ru(0001)<sup>15</sup>), a regular lattice of periodic hills and valleys spontaneously forms due to lattice mismatch between graphene and the substrate.<sup>39,40</sup> The static mechanical responses of these graphene "nanodomes" (*i.e.*, wrinkles) have been characterized by atomic force microscopy,<sup>6</sup> and by experimentally varying substrate corrugation,<sup>41–43</sup> the evolution of elastic deformations and the magnitude of strain-induced wrinkling in graphene can be demonstrated by quantitative Raman analysis.<sup>29,40</sup> A second strategy, chemical functionalization of pristine graphene, introduces exotic atoms, molecules, and functional groups onto its surface to control wrinkling.<sup>18,26,44</sup> In particular, hydrogenation of graphene, *i.e.*, adding hydrogen to carbon atoms and therefore changing its hybridization from  $sp^2$  to  $sp^3$ , causes local lattice deformation and might help to address the challenge of fabricating programmable graphene-based metamaterials and nanodevices.<sup>17,26</sup> Theoretically, static mechanical analysis based on continuum mechanics<sup>45–47</sup> and molecular dynamics (MD) simulations<sup>8,20</sup> can confirm the microscopic structure and strain-dependence of the wrinkling of graphene induced by chemical functionalization.

In addition to the two strategies described above, control of graphene wrinkling by adding defects offers a promising strategy for enabling novel devices.<sup>28,48</sup> Specifically, topological defects, such as dislocations<sup>25,49</sup> and disclinations<sup>50,51</sup> in crystals, can break the translational invariance of lattice symmetry and lead to warping and surface wrinkling with Gaussian curvature. Such defects unavoidably arise during fabrication of graphene, including by chemical vapor deposition (CVD)<sup>52,53</sup> and scanning focused electron-beam irradiation.<sup>25</sup> Actually, defect-induced wrinkling represents a classic problem in thin

<sup>a</sup> National Key Laboratory of Science and Technology on Advanced Composites in Special Environments, Harbin Institute of Technology, Harbin 150001, P. R. China. E-mail: wangcg@hit.edu.cn

<sup>b</sup> Center for Composite Materials and Structures, Harbin Institute of Technology, Harbin 150001, P. R. China

<sup>†</sup> Electronic supplementary information (ESI) available. See DOI: 10.1039/d1cp01254a

<sup>‡</sup> These authors contributed equally to this work.

film mechanics.<sup>52</sup> Several theoretical and experimental studies have reported on how the fundamental mechanics of graphene wrinkling are affected by topological defects, including point defects,<sup>54,55</sup> inverse Stone Wales (SW) defects,<sup>48,56</sup> dislocations,<sup>25,49</sup> disclinations,<sup>50,51</sup> and straight graphene grain boundaries (GBs)<sup>57–59</sup> in mono- and polycrystalline graphene. The duality of defects in graphene suggests that wrinkling can be controlled to produce delicate and desirable static and dynamic surface morphologies at GBs of various curvatures.<sup>54,60</sup> The presence of defects, for example, graphene with curved GBs<sup>61</sup> (see Fig. S1 (scanning tunnel microscope (STM) topographic images) in ESI† Appendix for details), poses critical questions about their effects on the dynamic mechanical behavior of graphene monolayers, including dynamic morphology, time dependence of out-of-plane displacement and energy, and dynamic defect shielding. As far as we know, however, this issue has yet to be adequately studied. The only closely related study focused on graphene sheets in which point defects, inverse Stone Wales defects, or line notches were introduced to guide the propagation of wrinkles,<sup>56</sup> and so did not address the dynamic nature and time dependence of the effects of GB curvature.

In the present work, we systematically studied wrinkle propagation in graphene with flower-like rotational GBs induced by C60 molecules, and the potential roles of GBs with various curvatures in the shielding and detection of defects. The following sections are organized as follows. Section 2 provides the design strategy inspired by experimental studies and illustrates the simulation methodology for the model. Section 3 delineates wrinkle propagation in pristine graphene and graphene sheets containing various flower-like GBs. For pristine graphene modeled as a nonlocal continuum plate, a contact law based on continuum mechanics was designated to investigate the nanoscale interactions. For graphene GBs of

various curvatures undergoing internal and external excitation, the out-of-plane displacement field, z-direction velocity, instantaneous atomic kinetic energy, and instantaneous atomic strain energy were systematically studied. The results revealed the regulation of directionality for dynamic wrinkles and their dependence on curvature. Furthermore, defect shielding was observed and a theoretical foundation for defect detection was revealed. Finally, Section 4 provides some concluding remarks.

## 2. Model and methodology

Classical molecular dynamics simulations were implemented through the large-scale atomic/molecular massively parallel simulator (LAMMPS).<sup>62</sup> The adaptive intermolecular reactive empirical bond order (AIREBO) potential was executed in the LAMMPS to describe the interatomic interaction among carbon atoms (see Note 2 in the ESI† Appendix for details). For the parameter of short-ranges REBO potential in AIREBO potential functions, the cutoff distance is adjusted to 2.0 Å to avoid the spurious strengthening effects far beyond the initial elastic region<sup>63</sup> as suggested by Shenderova *et al.*<sup>64</sup> Additionally, it is important to note that the Lennard-Jones term in AIREBO should be turned on to describe the corresponding interatomic van der Waals (vdW) interaction.

In our work, the model used to simulate pristine graphene contained 9660 carbon atoms with a length of 177.535 Å (armchair direction) and a width of 140.220 Å (zigzag direction), as shown in Fig. 1. The thickness of monolayer graphene is considered to be 3.35 Å.<sup>65</sup> The atoms at four edges were fixed with a length of 5 Å. The interaction between a C60 molecule and the graphene sheet was carried out in an NVE ensemble at a temperature of 5 K for 10 ps. The time step for the MD simulations

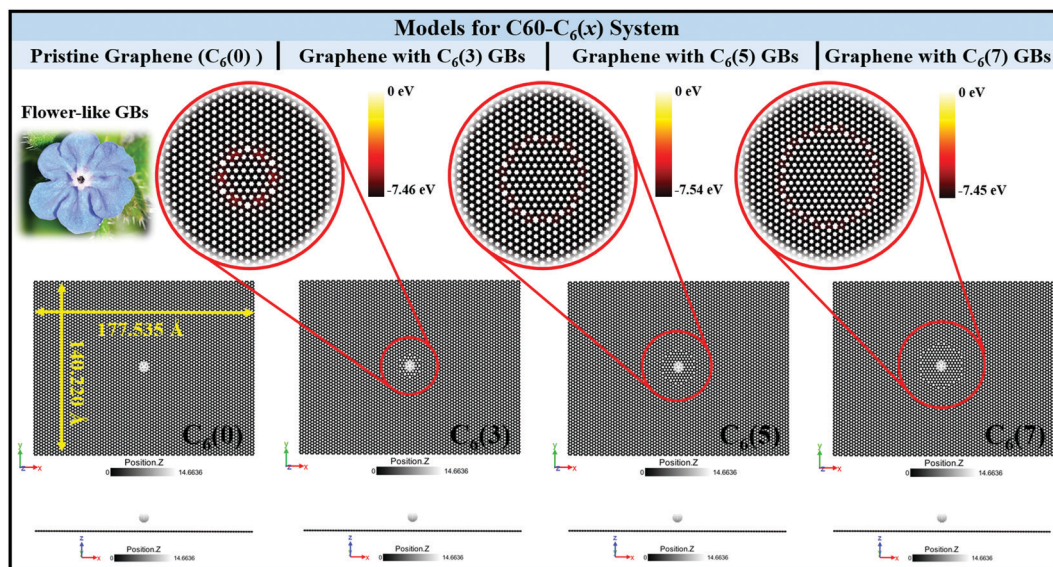


Fig. 1 Schematic illustration of the MD models for the C60–C<sub>6</sub>(x) system, where x = 0, 3, 5, 7. The red solid circles highlight the flower-like rotational GBs. A C60 molecule was placed 8 Å above the graphene sheet and the impact point was located in the center of the rotational GBs. Atoms are color coded according to their potential energies.

was chosen to be 1 fs. During the interaction phase, a Berendsen thermostat was utilized to control the temperature of the graphene sheet in the simulations. At the start of the simulation, a C<sub>60</sub> molecule located 8 Å above the graphene sheet moved toward the sheet at an initial vertical velocity of 15 Å ps<sup>-1</sup>.

Graphene sheets with various flower-like grain boundaries (*i.e.*, rotational GBs)<sup>61,65</sup> were constructed to study their effects on wrinkle propagation (Fig. 1). C<sub>6</sub>(*m,n*)<sub>|m=n</sub> describes a series of flower-like rotational GBs containing pentagonal, hexagonal and heptagonal carbon atom structures. The geometric parameters *m* and *n* are radially related to the size of the rotated patch. The central flower-like region rotated through an angle of  $\pi/(3m + 3n)$  (*i.e.*, 30°). C<sub>6</sub>(2*m* - 1) is used to represent the flower-like curvature GBs. Three types of flower-like rotational GBs, C<sub>6</sub>(3), C<sub>6</sub>(5), and C<sub>6</sub>(7), are introduced along the central axes of the graphene sheets in the armchair direction, as illustrated in Fig. 1. For C<sub>6</sub>(3), C<sub>6</sub>(5), and C<sub>6</sub>(7) GBs, the diameters of the defects were 22 Å, 29 Å, and 39 Å, respectively. In addition, 9659, 9660, and 9636 carbon atoms were contained within the graphene sheets with C<sub>6</sub>(3), C<sub>6</sub>(5), and C<sub>6</sub>(7) GBs, respectively. Specially, C<sub>6</sub>(0) was utilized to describe pristine graphene. The initial configurations used in the MD simulation are shown in Fig. 1.

### 3. Results and discussion

#### 3.1. Wrinkle propagation in pristine graphene

To study wrinkle propagation in pristine graphene, the dynamic evolution of the out-of-plane displacement field and

*z*-direction velocity were simulated as shown in Fig. 2a and b. Atomic snapshots of the out-of-plane displacement field were obtained from 250 fs to 2000 fs, with a time interval of 250 fs (Fig. 2a). Compared with the start of the simulation, the morphology of pristine graphene at 250 fs was almost unchanged as an extremely weak interaction exists between the C<sub>60</sub> molecule and pristine graphene. At 500 fs, a buckling bubble appeared and propagation of circular wrinkles occurred. In Fig. 2a, white (see the region around the impact point) represents the peak value of the out-of-plane displacement field, indicating that the C<sub>60</sub> molecule bounced off the buckling graphene sheet prior to 1500 fs. Subsequently, the circular wrinkles reflected off the fixed edge (see the black dotted box at 2000 fs). Owing to this reflection, the out-of-plane displacement field became irregularly distributed (see 2000 fs). Fig. 2b illustrates the distribution of velocity in the *z*-direction from 250 fs to 2000 fs, with a time interval of 250 fs. The contours of the out-of-plane displacement field and *z*-direction velocity were similar, as shown in Fig. 2a and b. Additionally, the evolution of instantaneous atomic kinetic energy and strain energy are shown in Fig. S2a and b (see Note 3 in the ESI† Appendix for details).

To provide additional understanding of wrinkle propagation in pristine graphene, the contact law<sup>46</sup> based on continuum mechanics was used to study the interaction between a hollow-ball model of the C<sub>60</sub> molecule and pristine graphene modeled as a nonlocal continuum plate, as shown in Fig. S3a and b (see Note 4 in the ESI† Appendix). In current research, the pristine

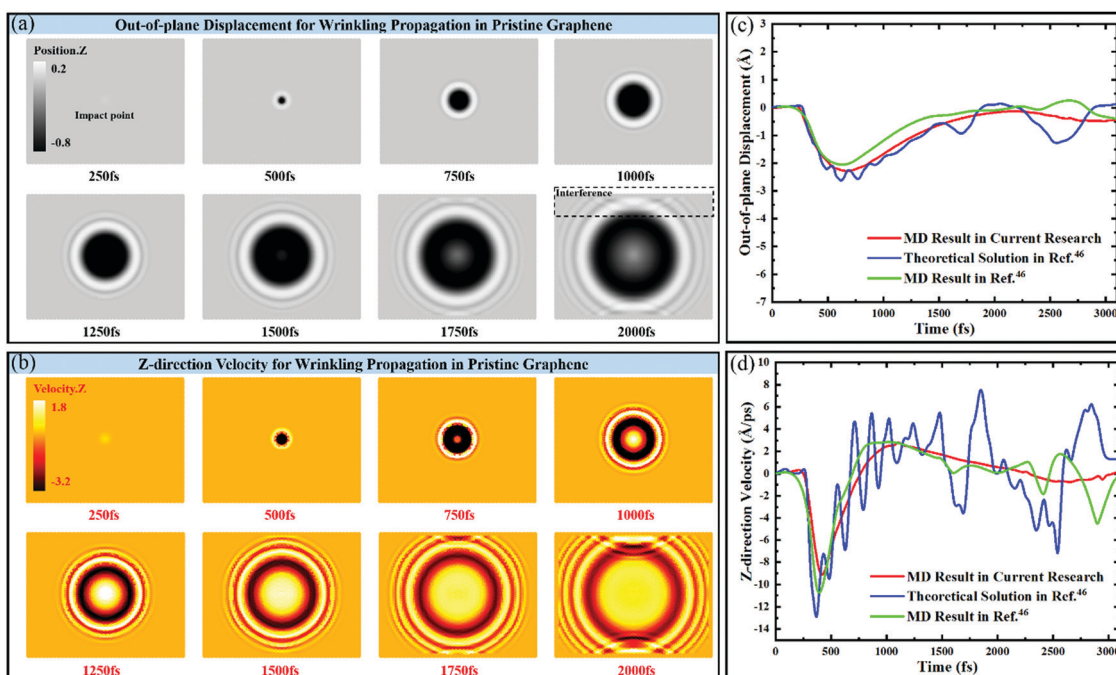


Fig. 2 Wrinkle propagation in pristine graphene induced by a C<sub>60</sub> molecule. Atomic snapshots are from 250 fs to 2000 fs, with a time span of 250 fs. (a) The distribution of the out-of-plane displacement field in Å units. Atoms are color coded with dark mapped to the lowest value. (b) The distribution of *z*-direction velocity in units of Å ps<sup>-1</sup>. Atoms are color coded with white mapped to the highest value. (c) Comparison of the out-of-plane displacement curves at the point of contact obtained from the current MD method (red line), the theoretical solution (blue line), and the former MD method (green line). (d) Comparison of *z*-direction velocity curves at the point of contact obtained using the different approaches.

graphene sheet was modeled by a plate with length, width, and thickness represented by  $a$ ,  $b$ , and  $h$ , respectively. Based on nonlocal theory of elasticity and Kirchhoff's assumptions,<sup>46,47,66</sup> the motion equation for a nonlocal plate can be given (see Note 4 in the ESI† Appendix), therefore, the out-of-plane displacement of the graphene,<sup>46</sup>  $w$ , can be obtained as:

$$w(x, y, t) = \sum_{i,j=1}^{\infty} \psi_{ij}(x, y)\eta_{ij}(t) \quad (1)$$

where,  $\psi_{ij}(x, y)$  are the mode shapes of vibrations and  $\eta_{ij}(t)$  are defined as the time-dependent coefficients for  $\psi_{ij}(x, y)$  (for details, see Note 4 in the ESI† Appendix).

The out-of-plane displacements of the plate at the point of contact  $(x_0, y_0) = (a/2, b/2)$  (*i.e.*, the center of plate) obtained via the MD method, the theoretical solution, and the former MD method<sup>46</sup> are compared in Fig. 2c. It can be seen that there was general agreement among these approaches. According to the approximate displacement amplitudes, this agreement indicates a similar energy transformation using these different approaches during the interaction phase, *i.e.*, the kinetic energy of the C<sub>60</sub> molecule can be converted into a similar strain energy in a pristine graphene sheet. Furthermore, the velocity can be attained by the derivation of  $w$  in terms of time. Fig. 2d illustrates the z-direction velocity at the point of contact obtained in the same way. The agreement between the quantities (see Fig. 2d) obtained by these different approaches is acceptable, and demonstrates a similar rate of energy transformation using these different approaches.

### 3.2. Wrinkle propagation across the curvature boundaries by internal excitation

To obtain physical insights into wrinkle propagation associated with flower-like curvature boundaries and induced by internal excitation (*i.e.*, the impact point is the center of the GB), MD simulations of graphene sheets with various rotational GBs were performed. For defective graphene sheets (*i.e.*, graphene sheets with C<sub>6</sub>(3), C<sub>6</sub>(5), and C<sub>6</sub>(7) GBs), Fig. 3a–c reveal the dynamic evolution of the out-of-plane displacement field, z-direction velocity, and instantaneous atomic kinetic and strain energies, respectively. Atomic snapshots ranged from 250 fs to 2000 fs, with a time span of 250 fs. Generally, the flower-like GBs can have a significant effect on wrinkle propagation. Specifically, the defective graphene sheets kept almost flat due to the weak interaction between the C<sub>60</sub> molecule and defective graphene (see the distributions of out-of-plane displacement field and z-direction velocity at 250 fs in Fig. 3a–c). The distributions of instantaneous atomic kinetic energy and strain energy presented hexagonal contours (see the distributions of instantaneous atomic kinetic and strain energies at 250 fs in Fig. 3a–c). The peak of instantaneous atomic strain energy always occurred in the region around the impact point in the whole simulations. The small bubble could be observed and the propagation of wrinkles began at 500 fs in Fig. 3a–c. At 1500 fs, the region around the impact point of defective graphene bounced (see white part at 1500 fs in Fig. 3a–c). The hexagonal

wrinkles reflected off the fixed edge (see 2000 fs in Fig. 3a–c). Unlike the circular wrinkles observed in pristine graphene (see Fig. 2a and b), hexagonal contours of wrinkle propagation were observed in the defective graphene sheets (see Fig. 3). Specifically, “flower-like” contours could be observed to evolve in graphene sheets with C<sub>6</sub>(5) and C<sub>6</sub>(7) GBs (see 1000–2000 fs in Fig. 3b and c). It is worth noting that, for the distributions of instantaneous atomic strain energy in Fig. 3a–c, atomic fluctuation around flower-like GBs can be responsible for the distinct differences compared with the distributions of the instantaneous atomic strain energy in pristine graphene (see Fig. S2b in the ESI† Appendix for details). Interestingly, an obvious discontinuous wrinkling configuration can be observed in Fig. 3c (see 2000 fs). This indicates a defect-shielding effect of flower-like rotational GBs on wrinkle propagation. Based on this effect, the graphene sheets with flower-like GBs might be useful in designs of graphene-based nanodevices such as protectors and shock absorbers.<sup>18,56,67,68</sup>

To investigate the in-plane evolution of wrinkle propagation for graphene sheets with various flower-like GBs, the time dependence of the variations for specific atomic x- and y-coordinates are shown in Fig. 4 (and Fig. S5 in the ESI† Appendix). Here, a polar coordinate system (see the  $r$ - $\theta$  coordinate system and atomic positions in Fig. S4 in the ESI† Appendix for details) was constructed to illustrate the evolution of specific atomic positions (*i.e.*, atom-a to atom-f). Generally, a significant curvature dependence of wrinkle propagation in the graphene sheets was observed, as shown in Fig. 4a–h (green, light green, light red, and red lines represent the four types of graphene sheets). Specifically, Fig. 4a–d depict changes in specific atomic x-coordinates with time. For the  $(r, 0)$  axis in the graphene sheets, moderate atomic fluctuations occur (see Fig. 4a: atom-a with  $(r, \theta) = (30, 0)$ , and see Fig. 4b: atom-b with  $(r, \theta) = (45, 0)$ ). For the  $(r, \pi/2)$  axis in graphene sheets with flower-like GBs, atomic fluctuation in Fig. 4c and d was magnified significantly as GB curvature decreased (from C<sub>6</sub>(3) to C<sub>6</sub>(7)). For pristine graphene, the atomic fluctuation was observed over a smaller range. For example, as shown in Fig. 4c,  $|x_{\max} - x_{\min}|$  in the graphene sheet with C<sub>6</sub>(7) GBs is 22 times larger than that of pristine graphene. Fig. 4a–d indicate that the in-plane propagation of wrinkles is dependent on curvature, *i.e.*, the regulation of directionality of wrinkle propagation can be achieved by changing the curvature of rotational GBs.

Moreover, Fig. 4e–h reveal the evolution of specific atomic y-coordinates for defective graphene sheets. Specifically, as shown in Fig. 4e–f, only a small atomic fluctuation occurs in pristine graphene. The atomic fluctuation of y-coordinates increases with increasing  $m$  in C<sub>6</sub>( $2m - 1$ ) (*i.e.*, with a decrease in GB curvature). For instance,  $|y_{\max} - y_{\min}|$  in the graphene sheet with C<sub>6</sub>(7) GBs is 1.6 times larger than that of pristine graphene in Fig. 4f. Similarly, Fig. 4g and h show a moderate atomic fluctuation over time. The obtained results in Fig. 4 can imply that the moderate atomic fluctuations occur in radial direction in polar coordinate, while the markedly atomic fluctuations can be observed in circumferential direction in polar coordinate. This can also indicate the flower-like GBs' ability of

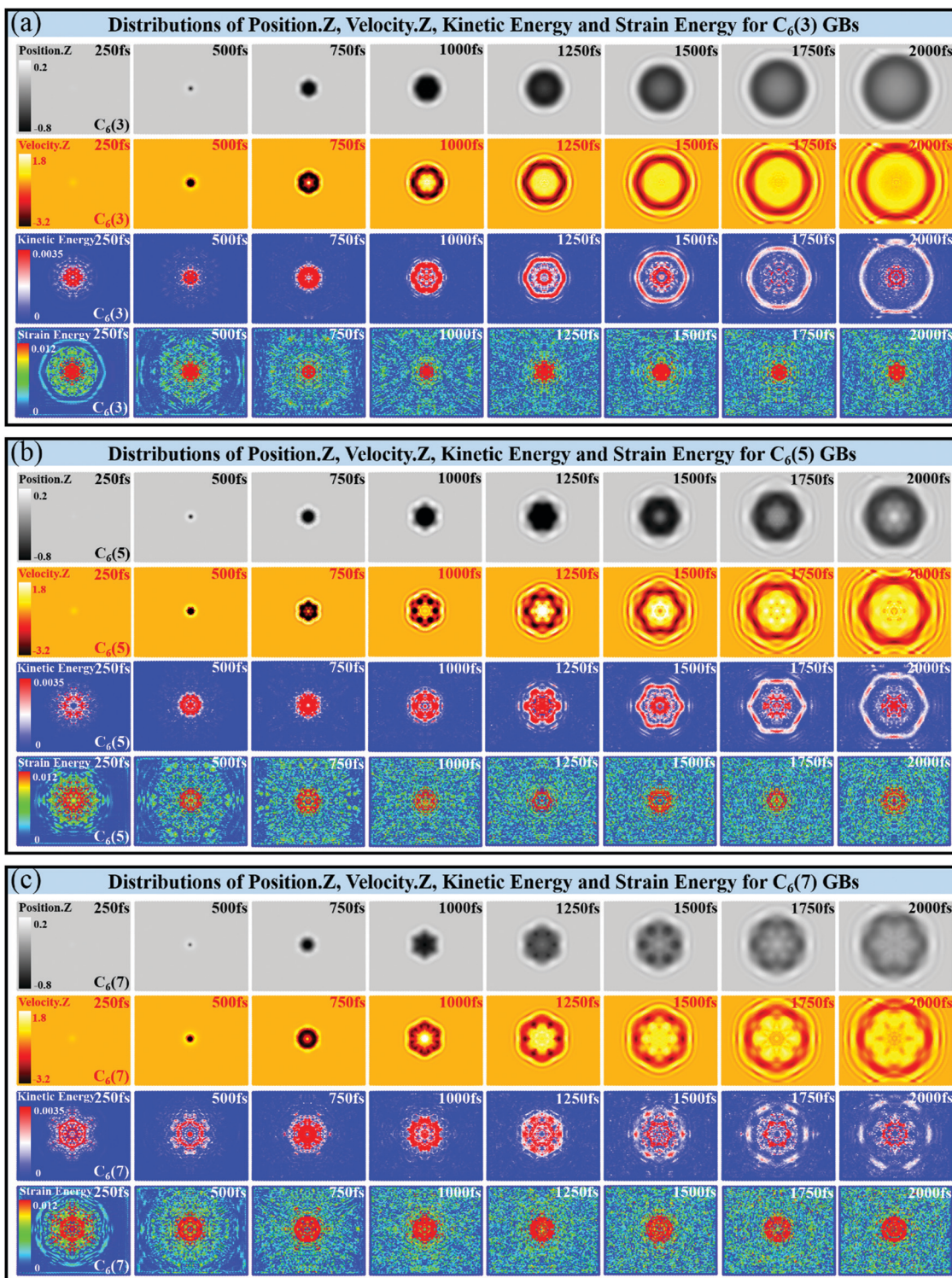


**Fig. 3** MD simulation results of defective graphene sheets induced by a  $C_{60}$  molecule. The distributions of the out-of-plane displacement field,  $z$ -direction velocity, instantaneous atomic kinetic energy, and instantaneous atomic strain energy in graphene sheets with (a)  $C_6(3)$ , (b)  $C_6(5)$ , and (c)  $C_6(7)$  GBs are shown. Atomic snapshots are from 250–2000 fs, with a time span of 250 fs. The units of displacement, velocity, and energy are  $\text{\AA}$ ,  $\text{\AA ps}^{-1}$ , and eV, respectively. According to their energies, atoms are color coded with blue mapped to the lowest value and red to the highest value.

directionality regulation for wrinkle propagation. To further illustrate the directionality of wrinkle propagation, the in-plane variations of  $x$ - and  $y$ -coordinates for the  $(r, \pi/4)$  axis are provided in Fig. S5a-d (see Note 6 in the ESI<sup>†</sup> Appendix).

Fig. S5 (ESI<sup>†</sup>) indicates that both  $x$ - and  $y$ -coordinates exhibit moderate atomic fluctuation, which is slightly different between atom-a and atom-b (see Fig. 4a-d and e-h). These results suggest an approach to regulation of wrinkle

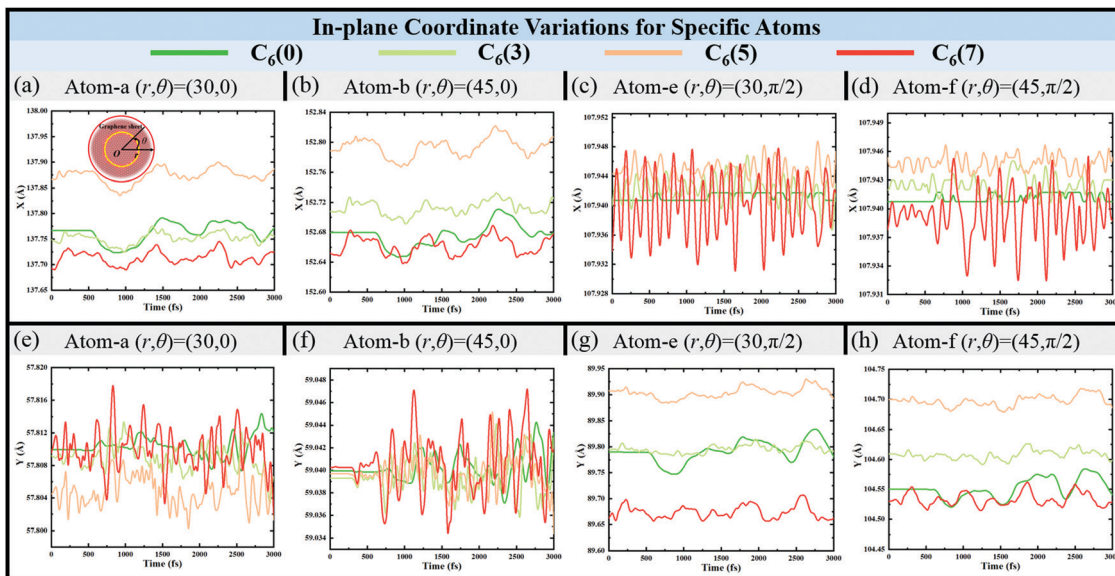


**Fig. 4** Variations in specific atomic positions for the  $(r, 0)$  and  $(r, \pi/2)$  axes. The polar coordinate system  $(r, \theta)$  is constructed.  $x$ -coordinate variations of (a) atom-a  $(r, \theta) = (30, 0)$ , (b) atom-b  $(r, \theta) = (45, 0)$ , (c) atom-e  $(r, \theta) = (30, \pi/2)$ , and (d) atom-f  $(r, \theta) = (45, \pi/2)$ .  $y$ -Coordinate variations of (e) atom-a  $(r, \theta) = (30, 0)$ , (f) atom-b  $(r, \theta) = (45, 0)$ , (g) atom-e  $(r, \theta) = (30, \pi/2)$ , and (h) atom-f  $(r, \theta) = (45, \pi/2)$ .

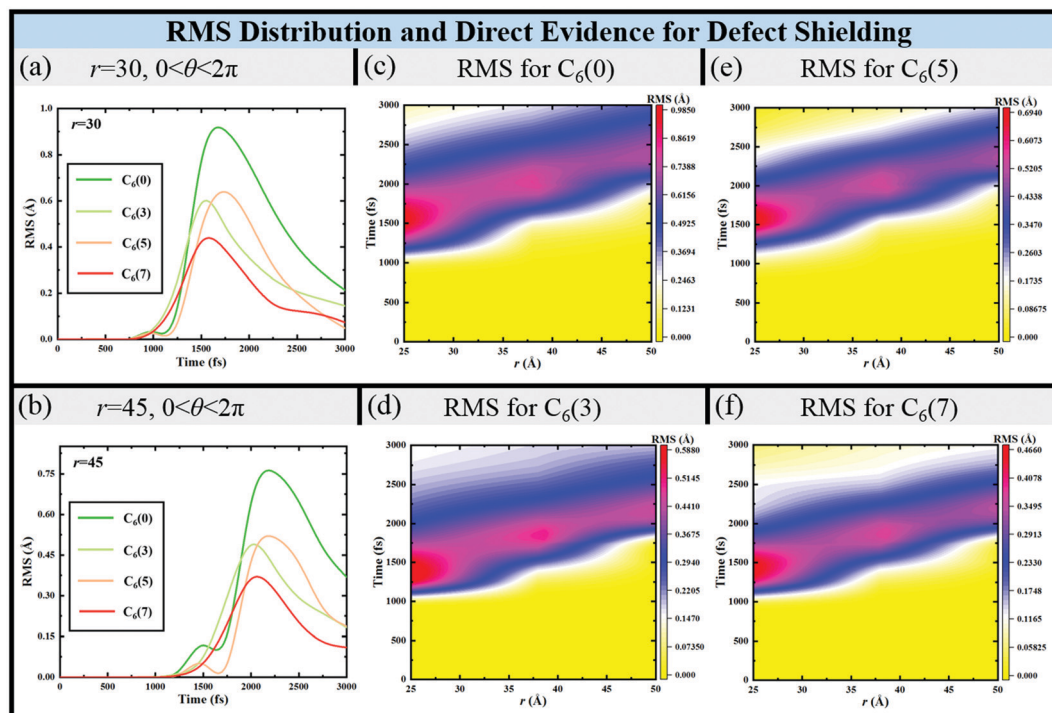


**Fig. 5** The distributions of RMS displacement in the  $z$  direction over time (from 0 fs to 3000 fs) and  $r$ -coordinate (from 25 Å to 50 Å) in the  $r-\theta$  polar coordinate. (a) and (b) show the evolution of RMS displacement values over time for  $r = 30$  Å and  $r = 45$  Å, respectively. (c) to (f) show the RMS displacement distributions for pristine graphene and the graphene sheets with  $C_6(3)$ ,  $C_6(5)$ , and  $C_6(7)$  GBs, respectively. The unit of RMS displacement is Å. RMS displacement is color coded with yellow representing the lowest value and red the highest value.

propagation in graphene sheets, including those with Stone Wales (SW) defects and vacancies,<sup>56</sup> and at graphene–boron nitride superlattice interfaces.<sup>31</sup>

To investigate the dynamic influence of flower-like curvature GBs on the out-of-plane displacement field and their

defect shielding effect, the evolution of  $z$ -direction fluctuations over time was studied. Out-of-plane deformations at the micro- and nano-scales are partially described by root mean square (RMS) displacement<sup>69</sup> in the  $z$ -direction in polar coordinates. Typical RMS displacements can be calculated

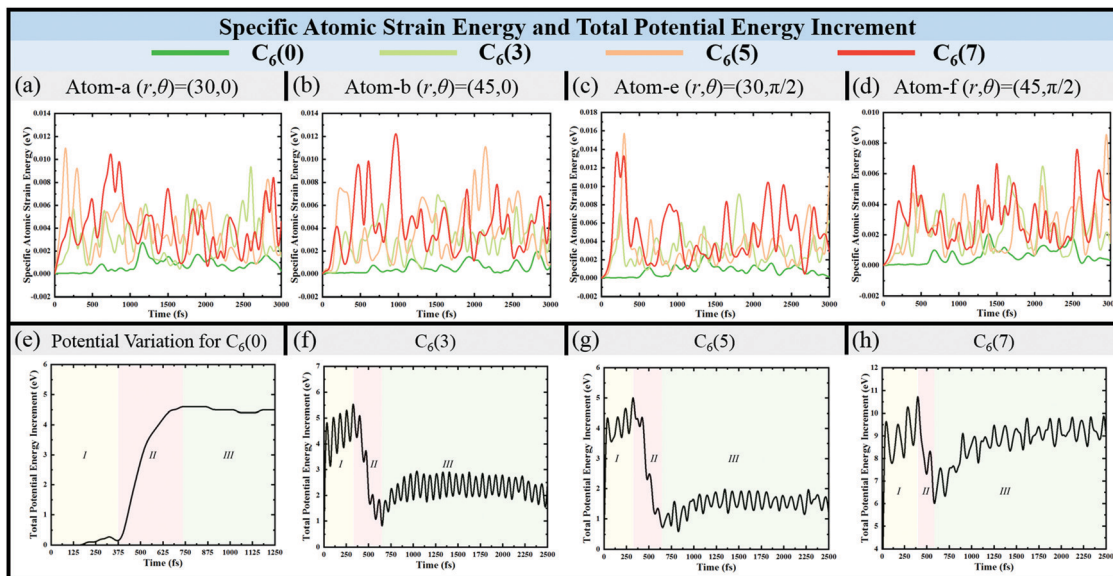


**Fig. 6** Evolution of increments in specific atomic strain energy and total potential energy. Specific atomic strain energies are plotted for (a) atom-a ( $r, \theta = (30, 0)$ ), (b) atom-b ( $r, \theta = (45, 0)$ ), (c) atom-e ( $r, \theta = (30, \pi/2)$ ), and (d) atom-f ( $r, \theta = (45, \pi/2)$ ) in the graphene sheets. Evolution of total potential energy increments are plotted for (e) pristine graphene, (f) graphene with  $C_6(3)$  GBs, (g) graphene with  $C_6(5)$  GBs, and (h) graphene with  $C_6(7)$  GBs. Energy is in units of eV.

using the following relationship:

$$\text{RMS} = \sqrt{\frac{\sum_{i=1}^n \Delta z_i^2}{n}} \quad (2)$$

where  $\Delta z_i$  and  $n$  represent the atomic  $z$ -direction displacement and the number of the atoms, respectively. In MD simulations, the sampling time was 3000 fs and the  $r$ -coordinate ranged from 25 Å to 50 Å. According to eqn (2), the evolution of RMS displacement with respect to time and  $r$ -coordinate is illustrated in Fig. 5c–f (the color bar is a scale of RMS displacement). In general, Fig. 5 demonstrates the directionality of wrinkle propagation and the significant defect-shielding effect of flower-like curvature GBs. Fig. 5a and b show RMS displacement values for  $r = 30$  Å and  $r = 45$  Å. The amplitudes of RMS displacement for defective graphene sheets were less than those of pristine graphene. In addition, maximum RMS displacement (0.9850 Å) occurred at  $(25, \theta)$  for pristine graphene (see 1500 fs in Fig. 5c). For the defective graphene sheets in Fig. 5d–f, the RMS displacement values were 0.588 Å, 0.694 Å, and 0.466 Å, respectively. Compared with pristine graphene, the RMS displacement values for the graphene sheets with  $C_6(3)$ ,  $C_6(5)$ , and  $C_6(7)$  GBs decreased 40.3%, 29.5%, and 52.7%, respectively. This strongly implies a duality of annular defects and demonstrates an obvious decrease in out-of-plane deformation. These results suggest an approach to defect shielding, and might also be useful for tuning thermal transport.<sup>44,60,70</sup>

To further understand wrinkle fluctuation and gain physical insight into defect shielding, we investigated atomic strain

energies for specific atoms and total potential energy of the graphene sheets. Fig. 6a–d describe the evolution of atomic strain energies for specific atoms (see atom-a, atom-b, atom-e, and atom-f in Fig. 6a–d, and atom-c and atom-d in Fig. S6a–d in the ESI† Appendix). Gradient lines are colored as shown in the insert. The increments of total potential energy for the graphene sheets are plotted in Fig. 6e–h. Specifically, for the defective graphene sheets, their specific atomic strain energies increased significantly, as shown in Fig. 6a–d. This indicates that the carbon–carbon bond length increased significantly and the bond angle rotated markedly. This might also imply that the specific atomic strain energies are magnified significantly by GB curvature. Out-of-plane deformations can be partially transformed into in-plane fluctuations through local deformation and rotation of curved GBs.

Increments in total potential energy of the graphene sheets demonstrated two different evolution modes: (i) For the pristine graphene in Fig. 6e, the potential energy increment was unchanged from the start of the simulation to 175 fs. Then, a slight fluctuation occurred (see phase I in the figure). At 375 fs, the curve rose markedly (see phase II). Subsequently, a slight decrease occurred at 875 fs. Finally, moderate fluctuation was observed (see phase III). (ii) For defective graphene sheets (see Fig. 6f–h), in phase I, the potential energy increments increased rapidly owing to the fixed boundary condition during relaxation. Then a significant decrease occurred in phase II. The minimum value occurred at about 650 fs (see Fig. 6f, for example). After a moderate rise, a steady fluctuation was observed (see phase III in the figures). Actually, the conversion of energies (including the kinetic and potential energies of the  $C_60$  molecule and graphene sheet, as well as the van der Waals (vdW) potential energy between them) can explain the

two different evolution modes. For example, the kinetic energy of the C<sub>60</sub> molecule decreased after 175 fs in pristine graphene. At the same time, the C<sub>60</sub> molecule interacted with the graphene sheet. Then most of the kinetic energy of the C<sub>60</sub> molecule was converted into kinetic and potential energies of pristine graphene. This led to a significant increase in the potential energy of the C<sub>60</sub> molecule and graphene sheet and the vdW potential energy between them (see Fig. S7a in the ESI† Appendix) at 400 fs. Subsequently, when the C<sub>60</sub> molecule bounced, the vdW potential energy decreased. Then the pristine graphene potential energy was continuously converted into kinetic energy and propagated in the form of fluctuating wrinkles. Finally, the total potential energy increment became relatively stable. However, for the defective graphene sheets, the initial out-of-plane perturbation increased with a decrease in curvature (*i.e.*, an increase in defect density). For example, the initial potential energy increment (~9.6 eV) in Fig. 6h approximated the kinetic energy of the C<sub>60</sub> molecule. This led to a significant decrease in the total potential energy increment. In other words, wrinkling fluctuation is partially shielded/offset by the initial perturbation of flower-like GBs. The potential energy of graphene sheets is converted into kinetic energy over time. Moreover, with interference and diffraction, the potential energy of the graphene sheet remains at a lower level. It is worth noting that the deformation of the C<sub>60</sub> molecule is very small, and the vdW potential energy can play an important role only during the interaction phase, as seen in Fig. S7a–d (see Note 8 in the ESI† Appendix). According to these results, two distinctly different modes of changes in energy can be used to explain defect shielding and defect

detection. To provide a more comprehensive understanding of these modes, snapshots of the out-of-plane displacement field, z-direction velocity, instantaneous atomic kinetic, and strain energies for point defects (single vacancy) and single SW defects (see Fig. S9 in the ESI† Appendix), as well as wrinkle propagation in the defective graphene sheets induced by external excitation (*i.e.*, the impact point outside the GBs, see Fig. 8), are provided in Section 3.3.

Finally, to obtain a full understanding of wrinkle propagation induced by internal excitation, we investigate the effects of initial velocity and temperature on out-of-plane displacement along the (*r*, 0) and (*r*, π/2) axes in polar coordinates. Fig. 7 shows the effects of different initial velocities (a–d: 15 Å ps<sup>-1</sup>, 30 Å ps<sup>-1</sup>, 45 Å ps<sup>-1</sup>, and 60 Å ps<sup>-1</sup>) and temperatures (e–h: 5 K, 25 K, 50 K, 75 K, and 100 K) on out-of-plane displacements for graphene sheets with C<sub>6</sub>(3) and C<sub>6</sub>(5) GBs at 1000 fs (see also the results in the ESI† Appendix for pristine and C<sub>6</sub>(7) GB graphene sheets in Fig. S8a–d (velocity) and e–h (temperature), ESI†). In general, Δz (out-of-plane displacement) increases with increasing initial velocity and temperature, although there were a few exceptions (see 45 Å ps<sup>-1</sup> and 60 Å ps<sup>-1</sup> in Fig. 7b, and 30 Å ps<sup>-1</sup>, 45 Å ps<sup>-1</sup>, and 60 Å ps<sup>-1</sup> in Fig. S8a and c, ESI†). Specifically, with increasing initial velocity, the out-of-plane displacement exhibited two modes: (i) at a low velocity (such as 15 Å ps<sup>-1</sup>), a "V" shape was observed (Fig. 7b), and (ii) when velocity was equal to or greater than 30 Å ps<sup>-1</sup> (such as 30 Å ps<sup>-1</sup>, 45 Å ps<sup>-1</sup>, and 60 Å ps<sup>-1</sup>), a "W" shape was observed. These results imply that, at higher velocity, the potential energy of the graphene sheet is transformed into kinetic energy more quickly, propagating in the form of the wrinkles. Moreover, the

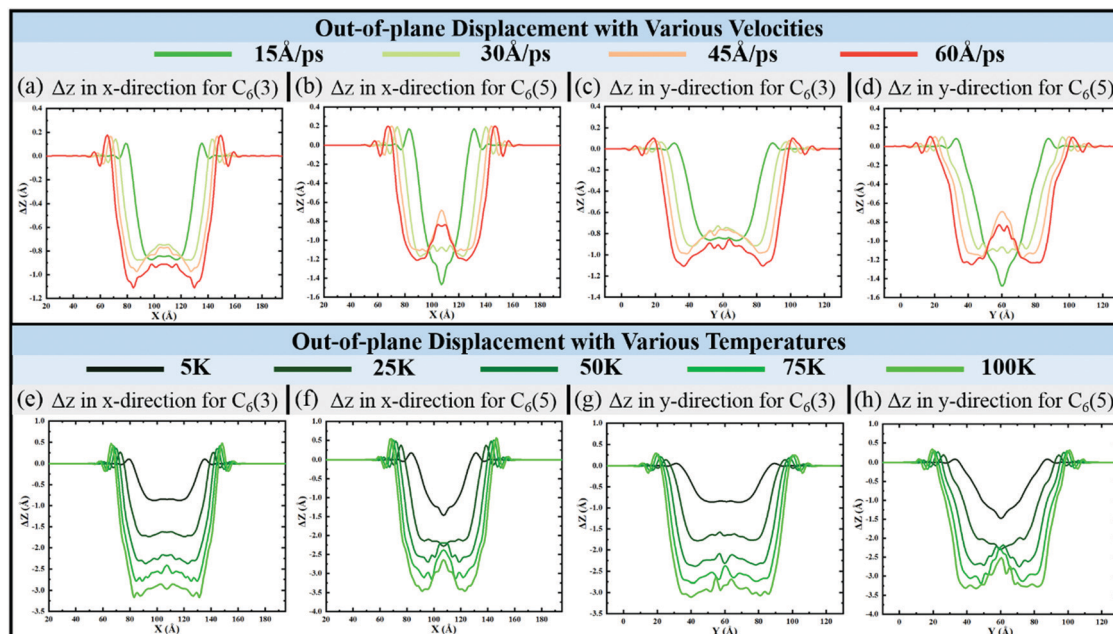


**Fig. 7** Out-of-plane displacements along the (*r*, 0) and (*r*, π/2) axes in polar coordinates with different initial velocities (15 Å ps<sup>-1</sup>, 30 Å ps<sup>-1</sup>, 45 Å ps<sup>-1</sup>, and 60 Å ps<sup>-1</sup>) and temperature variations (5 K, 25 K, 50 K, 75 K, and 100 K) at 1000 fs. (a)–(d) show the out-of-plane displacement (Δz) along the (*r*, 0) and (*r*, π/2) axes for graphene sheets with C<sub>6</sub>(3) and C<sub>6</sub>(5) GBs at different initial velocities. (e)–(h) show the out-of-plane displacement (Δz) along the (*r*, 0) and (*r*, π/2) axes for graphene sheets with C<sub>6</sub>(3) and C<sub>6</sub>(5) GBs at different temperatures. Displacement is in Å units.

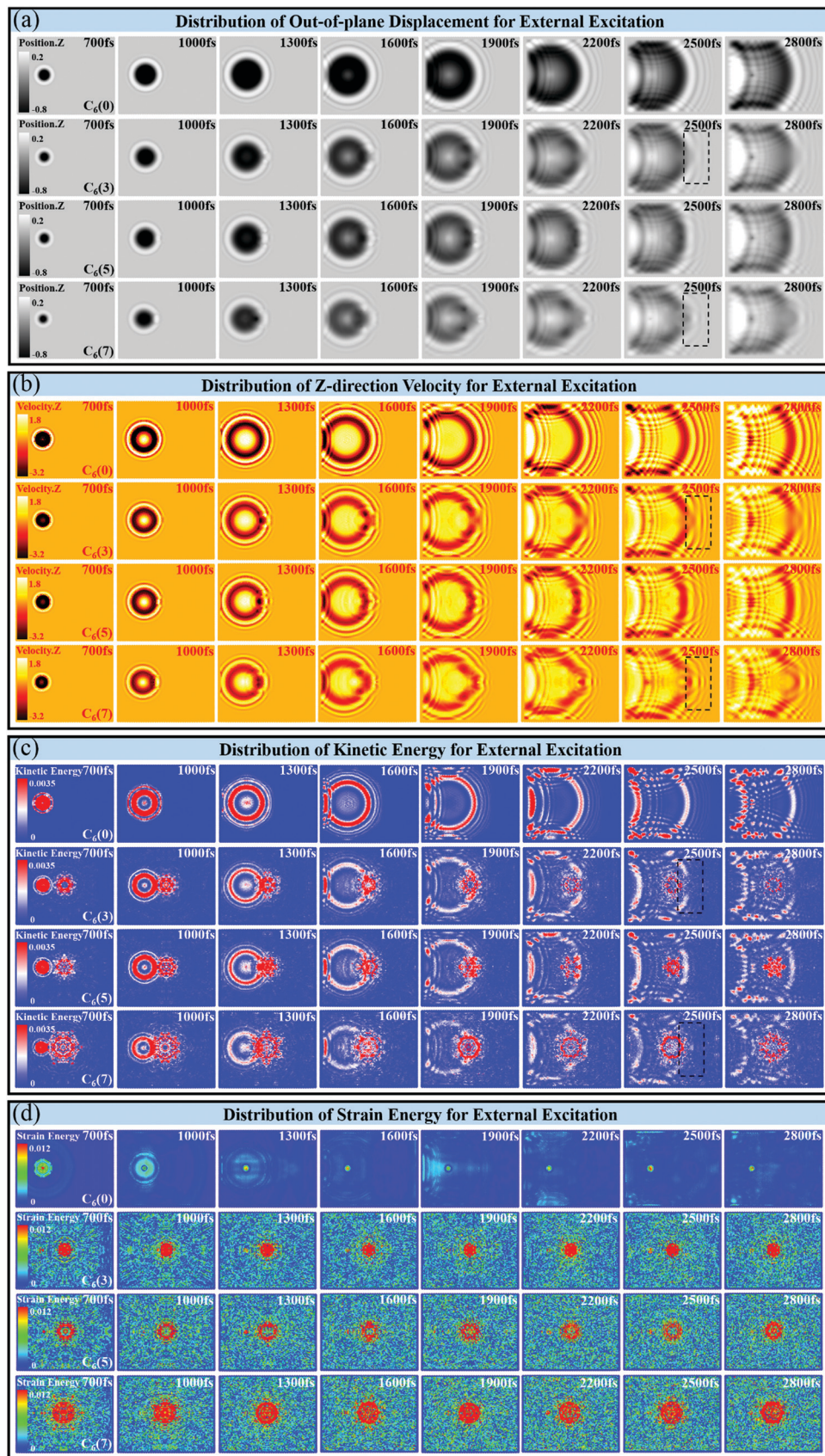


**Fig. 8** Wrinkle propagation through flower-like rotational GBs with external excitation. The distributions of (a) the out-of-plane displacement field, (b) z-direction velocity, (c) instantaneous atomic kinetic energy and (d) instantaneous atomic strain energy for pristine graphene and defective graphene sheets. Displacement, velocity and energy are in units of Å, Å ps<sup>-1</sup>, and eV, respectively.

system temperature was accurately controlled at 5 K in the current research, which is important for studying the temperature on wrinkle propagation. As shown in Fig. 7e–h, conversion between potential and kinetic energy can be accelerated at temperatures higher than 5 K (such as 75 K and 100 K). Owing to this conversion, a ‘W’ shape can be observed in the figures. In practice, these results indicate that different initial velocities and temperatures could contribute to dynamic surface regulation of related nanodevices, for example, in strain-based electronic devices,<sup>18,33,70</sup> high frequency nanoelectromechanical systems,<sup>71</sup> and nano-protector.<sup>56</sup>

### 3.3. Wrinkle propagation through flower-like rotational GBs: toward detection of defects

In graphene-based nanodevices, topological defects (point defects,<sup>54,55</sup> SW defects,<sup>48,56</sup> dislocations,<sup>25,49</sup> disclinations,<sup>50,51</sup> linear,<sup>57–59</sup> and curved GBs<sup>54,60,61,65</sup>) inevitably exist. Topological defects are generated during CVD growth,<sup>52,60</sup> ion beam irradiation<sup>25,68</sup> and by lattice mismatch,<sup>50,51,68</sup> which can be verified using a large number of experimental approaches. The results presented here allow for creation of a database for detection of defects based on the mechanism of wrinkle propagation (see flower-like rotational GBs in Fig. 8, and point and SW defects in Fig. S9 in the ESI† Appendix). Wrinkle propagation through flower-like rotational GBs was investigated *via* the distribution of out-of-plane displacement fields (see Fig. 8a), z-direction velocity

fields (see Fig. 8b), and instantaneous atomic kinetic (see Fig. 8c) and strain energies (see Fig. 8d). These observations provide physical insights into defect detection for two dimensional materials with the curved defects.

Fig. 8 shows an impact point of  $(40, \pi)$  in polar coordinates. The colored bars in the first column (Fig. 8a–d) represent the out-of-plane displacement field, z-direction velocity, instantaneous atomic kinetic and strain energies, respectively. Generally, rotational GBs curvature will have a significant effect on the propagation of wrinkles across defects. Specifically, when the curvatures of wrinkles and flower-like GBs are mismatched (*e.g.*, the curvature of wrinkles is larger than that of the rotational GBs), the distributions of the out-of-plane displacement field, z-direction velocity field, and instantaneous atomic kinetic energy hinder wrinkling (see the black dotted box in Fig. 8a–c). However, when the curvatures of the wrinkles and rotational GBs are similar, dynamic wrinkles can cross the rotational GBs with unaltered morphology, as shown in Fig. 8a–d. In addition, wrinkle propagation in graphene sheets with point and SW defects helps to provide a fuller understanding of defect detection (see Fig. S9 in the ESI† Appendix for details). As can be seen in Fig. S9a and b (see Note 9 in the ESI† Appendix), distinctly different morphologies were observed at 1250 fs, which further suggests that dynamic wrinkling signals<sup>56,72</sup> can be used to detect defects in graphene.

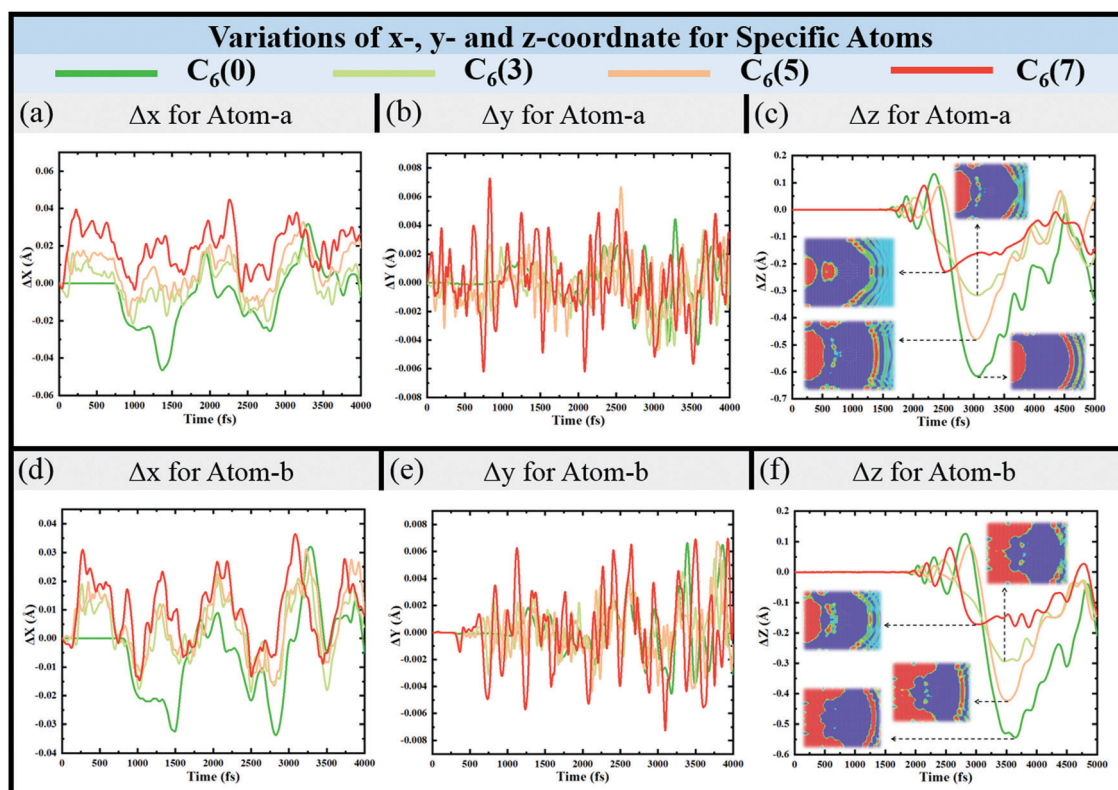


**Fig. 9** Displacements in the x-, y- and z-directions for specific atoms. (a)–(c) show the x-direction ( $\Delta x$ ), y-direction ( $\Delta y$ ), and z-direction ( $\Delta z$ ) displacements for atom-a, while (d)–(f) show the same for atom-b. The unit of displacement is Å. Snapshots corresponding to the maximum amplitudes of out-of-plane displacements in the graphene sheets are shown in (c) and (f).

To obtain a full understanding of the mechanism of wrinkle propagation through flower-like rotational GBs for purposes of defect detection requires knowledge of the evolution of  $x$ -direction ( $\Delta x$ ),  $y$ -direction ( $\Delta y$ ),  $z$ -direction ( $\Delta z$ ) displacements for atom-a and atom-b (see Fig. 9a–f), as well as specific atomic strain energy, total potential energy increment, and vdW potential energy (see Fig. S10a–j in the ESI† Appendix for details). Specifically, for  $\Delta x$  of atom-a in Fig. 9a, similar maximum amplitudes of the four graphene sheets were observed. Similar results are shown in Fig. 9b and d, e. In addition, Fig. 9c and f show the less significant out-of-plane wrinkle fluctuations for graphene sheets with GBs. This provides evidence for defect shielding by flower-like GBs. Fig. S10a, b (see Note 11 in the ESI† Appendix) show that the lowest atomic strain energy increment is observed for pristine graphene. The atomic strain energies of atom-a and atom-b in defective graphene sheets increase over time. That is, the smaller the curvature of rotational GBs, the greater the change in bond length and angle. Moreover, two modes of temporal evolution of total potential energy increment are shown in Fig. S10c–f (see Note 11 in the ESI† Appendix), which are the same modes as in Fig. 6e–h. For defective graphene sheets, total potential energy decreased significantly owing to the conversion of potential energy into atomic kinetic energy. During interactions between the C<sub>60</sub> molecule and graphene sheet, the vdW potential energy decreased and then increased (see Fig. S10g–j in the ESI† Appendix for details).

Furthermore, out-of-plane displacements along the ( $r, 0$ ) axis at different times (1200 fs, 1800 fs, 2400 fs, 3000 fs, and 3300 fs) are shown in Fig. S11a–d (see Note 12 in the ESI† Appendix). The amplitude of dynamic wrinkles generally decreased with time in the same graphene sheet. This indicates that out-of-plane deformation energy can be converted into in-plane perturbations. Specifically, as illustrated in Fig. S11a–d (see Note 12 in the ESI† Appendix), the minimum amplitudes were 0.581 Å, 0.308 Å, 0.447 Å and 0.164 Å at 3300 fs, respectively. The defect shielding effect should be further verified.

Although a comprehensive demonstration of wrinkle propagation has been provided here (internal excitation in Section 3.2, and external excitation in Section 3.3), there is still much room for improvement in studies of the propagation of wrinkles in polycrystalline graphene with rotational GBs. The author hopes to further pursue this question in the future.

## 4. Conclusions

In summary, we systematically developed an experimentally-based strategy to regulate wrinkle propagation by using flower-like rotational grain boundaries (GBs). We investigated wrinkle morphology during propagation in four types of graphene sheet (pristine, and with C<sub>6</sub>(3), C<sub>6</sub>(5), and C<sub>6</sub>(7) GBs). These results were used to construct a database of wrinkle propagation in defective graphene sheets with GBs of different rotational curvature. Five significant conclusions can be drawn:

(i) For pristine graphene, the MD simulation phase diagrams for the distributions of the out-of-plane displacement field,  $z$ -direction velocity, instantaneous atomic kinetic energy, and instantaneous atomic strain energy, and the corresponding contact law based on continuum mechanics, can form a theoretical basis for graphene-based nanodevices.

(ii) For wrinkle propagation across curved GBs using internal excitation (*i.e.*, the point of impact is at the center of flower-like GBs), curvature affects the phase diagrams for specific atomic  $x$ - and  $y$ -coordinate variations, out-of-plane displacement fields,  $z$ -direction velocities, and instantaneous kinetic and strain energies. For example, the maximum RMS displacements of out-of-plane displacement vary as C<sub>6</sub>(0) > C<sub>6</sub>(5) > C<sub>6</sub>(3) > C<sub>6</sub>(7).

(iii) For wrinkle propagation across curved GBs using external excitation (*i.e.*, the point of impact is outside the flower-like GBs), mismatch of the curvatures of the wrinkles and flower-like rotational GBs leads to a significant defect shielding/offsetting effect. Specifically, when their curvatures are similar, dynamic wrinkles can cross the flower-like rotational GBs without being shielded.

(iv) Characterizing energy transformation and dissipation can be vital for a full understanding of wrinkle propagation, and especially the defect-shielding effect.

(v) The insights gained from our observations of wrinkle propagation across flower-like rotational GBs using internal and external excitation raise the possibility of regulating both the direction of propagation and its dependence on GB curvature. This interaction between propagating wrinkles and GBs could provide a theoretical basis for construction of nanodevices in which defects can both be detected and shielded.

## Conflicts of interest

There are no conflicts to declare.

## Acknowledgements

This work was supported by National Natural Science Foundation of China, 11872160 and 11572099. The author would like to express his thanks to the editor and anonymous reviewers whose constructive comment significantly improved the paper.

## References

- 1 A. K. Geim and K. S. Novoselov, The Rise of Graphene, *Nat. Mater.*, 2007, **6**, 183–191.
- 2 Y. M. Lin, C. Dimitrakopoulos, K. A. Jenkins, D. B. Farmer, H. Y. Chiu, A. Grill and P. Avouris, 100-GHz transistors from wafer-scale epitaxial graphene, *Science*, 2010, **327**(5966), 662.
- 3 K. S. Novoselov, A. K. Geim, S. V. Morozov, D. Jiang, Y. Zhang, S. V. Dubonos, I. V. Grigorieva and A. A. Firsov, Electric field effect in atomically thin carbon films, *Science*, 2004, **306**(5696), 666–669.

- 4 Y. Wang, C. Wang and H. Tan, Intrinsic edge warping of graphene nanoribbon boost molecular directional motion: Toward the novel nanodevices, *Phys. Lett. A*, 2019, **383**(13), 1473–1477.
- 5 J. S. Bunch, A. M. van der Zande, S. S. Verbridge, I. W. Frank, D. M. Tanenbaum, J. M. Parpia, H. G. Craighead and P. L. McEuen, Electromechanical resonators from graphene sheets, *Science*, 2007, **315**(5811), 490–493.
- 6 S. Koch, D. Stradi, E. Gnecco, S. Barja, S. Kawai, C. Diaz, M. Alcami, F. Martin, A. L. Vazquez de Parga, R. Miranda, T. Glatzel and E. Meyer, Elastic response of graphene nanodomes, *ACS Nano*, 2013, **7**(4), 2927–2934.
- 7 U. Monteverde, J. Pal, M. A. Migliorato, M. Missous, U. Bangert, R. Zan, R. Kashtiban and D. Powell, Under pressure: Control of strain, phonons and bandgap opening in rippled graphene, *Carbon*, 2015, **91**, 266–274.
- 8 C. Feng, Z. Yi, L. F. Dumée, F. She, Z. Peng, W. Gao and L. Kong, Tuning micro-wrinkled graphene films for stretchable conductors of controllable electrical conductivity, *Carbon*, 2018, **139**, 672–679.
- 9 C. H. Park, L. Yang, Y. W. Son, M. L. Cohen and S. G. Louie, Anisotropic behaviours of massless Dirac fermions in graphene under periodic potentials, *Nat. Phys.*, 2008, **4**(3), 213–217.
- 10 S. Wu, M. Killi and A. Paramakanti, Graphene under spatially varying external potentials: Landau levels, magneto-transport, and topological modes, *Phys. Rev. B: Condens. Matter Mater. Phys.*, 2012, **85**, 195404.
- 11 A. H. Castro Neto, F. Guinea, N. M. R. Peres, K. S. Novoselov and A. K. Geim, The electronic properties of graphene, *Rev. Mod. Phys.*, 2009, **81**(1), 109–162.
- 12 A. Iorio and P. Pais, Revisiting the gauge fields of strained graphene, *Phys. Rev. D: Part., Fields, Gravitation, Cosmol.*, 2015, **92**, 125005.
- 13 F. Guan and X. Du, Random Gauge Field Scattering in Monolayer Graphene, *Nano Lett.*, 2017, **17**(11), 7009–7014.
- 14 A. Fasolino, J. H. Los and M. I. Katsnelson, Intrinsic ripples in graphene, *Nat. Mater.*, 2007, **6**, 858–861.
- 15 A. L. Vázquez de Parga, F. Calleja, B. Borca, M. C. G. Passeggi Jr., J. J. Hinarejos, F. Guinea and R. Miranda, Periodically rippled graphene growth and spatially resolved electronic structure, *Phys. Rev. Lett.*, 2008, **100**(5), 23–28.
- 16 A. T. N'Diaye, S. Bleikamp, P. J. Feibelman and T. Michely, Two-dimensional Ir cluster lattice on a graphene moire on Ir(111), *Phys. Rev. Lett.*, 2006, **97**(21), 215501.
- 17 C. Chen, S. Rosenblatt, K. I. Bolotin, W. Kalb, P. Kim, I. Kymissis, H. L. Stormer, T. F. Heinz and J. Hone, Performance of monolayer graphene nanomechanical resonators with electrical readout, *Nat. Nanotechnol.*, 2009, **4**(12), 861–867.
- 18 R. Miranda and A. L. Vazquez de Parga, Surfing ripples towards new devices, *Nat. Nanotechnol.*, 2009, **4**(9), 549–550.
- 19 A. F. Fonseca, S. O. Dantas, D. S. Galvao, D. Zhang and S. B. Sinnott, The structure of graphene on graphene/C<sub>60</sub>/Cu interfaces: a molecular dynamics study, *Nanotechnology*, 2019, **30**(50), 505707.
- 20 P. Kumar H. G., S. Prabhakaran, A. Xavior M., S. Kalainathan, D. Lin, P. Shukla and V. K. Vasudevan, Enhanced surface and mechanical properties of bioinspired nanolaminate graphene-aluminum alloy nanocomposites through laser shock processing for engineering applications, *Mater. Today Commun.*, 2018, **16**, 81–89.
- 21 S. Chun, Y. Choi and W. Park, All-graphene strain sensor on soft substrate, *Carbon*, 2017, **116**, 753–759.
- 22 S. Zhao, Y. Zhang, J. Yang and S. Kitipornchai, Improving interfacial shear strength between graphene sheets by strain-induced wrinkles, *Carbon*, 2020, **168**, 135–143.
- 23 P. J. Lynch, S. P. Ogilvie, M. J. Large, A. A. Graf, M. A. O'Mara, J. Taylor, J. P. Salvage and A. B. Dalton, Graphene-based printable conductors for cyclable strain sensors on elastomeric substrates, *Carbon*, 2020, **169**, 25–31.
- 24 G. López Polín, M. Jaafar, F. Guinea, R. Roldán, C. Gómez Navarro and J. Gómez Herrero, The influence of strain on the elastic constants of graphene, *Carbon*, 2017, **124**, 42–48.
- 25 J. H. Warner, Y. Fan, A. W. Robertson, K. He, E. Yoon and G. D. Lee, Rippling graphene at the nanoscale through dislocation addition, *Nano Lett.*, 2013, **13**(10), 4937–4944.
- 26 D. C. Elias, R. R. Nair, T. M. Mohiuddin, S. V. Morozov, P. Blake, M. P. Halsall, A. C. Ferrari, D. W. Boukhvalov, M. I. Katsnelson, A. K. Geim and K. S. Novoselov, Control of graphene's properties by reversible hydrogenation: evidence for graphane, *Science*, 2009, **323**(5914), 610–613.
- 27 X. Li, W. Yang, K. Luo and Z. Wu, Tunable anisotropic behaviors in phosphorene under periodic potentials in arbitrary directions, *Nanotechnology*, 2019, **31**(10), 105205.
- 28 Y. Wang and C. Wang, Self-assembly of graphene sheets actuated by surface topological defects: Toward the fabrication of novel nanostructures and drug delivery devices, *Appl. Surf. Sci.*, 2020, **505**, 144008.
- 29 Y. Zhang, M. Heiranian, B. Janicek, Z. Budrikis, S. Zapperi, P. Y. Huang, H. T. Johnson, N. R. Aluru, J. W. Lyding and N. Mason, Strain Modulation of Graphene by Nanoscale Substrate Curvatures: A Molecular View, *Nano Lett.*, 2018, **18**(3), 2098–2104.
- 30 W. Bao, F. Miao, Z. Chen, H. Zhang, W. Jang, C. Dames and C. N. Lau, Controlled ripple texturing of suspended graphene and ultrathin graphite membranes, *Nat. Nanotechnol.*, 2009, **4**(9), 562–566.
- 31 D. Nandwana and E. Ertekin, Ripples, strain, and misfit dislocations: structure of graphene-boron nitride superlattice interfaces, *Nano Lett.*, 2015, **15**(3), 1468–1475.
- 32 F. Guinea, M. I. Katsnelson and A. K. Geim, Energy gaps and a zero-field quantum Hall effect in graphene by strain engineering, *Nat. Phys.*, 2009, **6**(1), 30–33.
- 33 T. Low and F. Guinea, Strain-induced pseudomagnetic field for novel graphene electronics, *Nano Lett.*, 2010, **10**(9), 3551–3554.
- 34 B. Amorim, A. Cortijo, F. de Juan, A. G. Grushin, F. Guinea, A. Gutiérrez-Rubio, H. Ochoa, V. Parente, R. Roldán, P. San-Jose, J. Schiefele, M. Sturla and M. A. H. Vozmediano, Novel effects of strains in graphene and other two dimensional materials, *Phys. Rep.*, 2016, **617**, 1–54.

- 35 S. T. Gill, J. H. Hinnefeld, S. Zhu, W. J. Swanson, T. Li and N. Mason, Mechanical Control of Graphene on Engineered Pyramidal Strain Arrays, *ACS Nano*, 2015, **9**(6), 5799–5806.
- 36 J. C. Spear, J. P. Custer and J. D. Batteas, The influence of nanoscale roughness and substrate chemistry on the frictional properties of single and few layer graphene, *Nanoscale*, 2015, **7**(22), 10021–10029.
- 37 G. Amato, Properties and applications of graphene membranes grown on Co, *Mater. Today: Proc.*, 2020, **20**, 1–6.
- 38 L. Li, Y. Dong, W. Guo, F. Qian, F. Xiong, Y. Fu, Z. Du, C. Xu and J. Sun, High-responsivity photodetectors made of graphene nanowalls grown on Si, *Appl. Phys. Lett.*, 2019, **115**, 081101.
- 39 D. Nandwana and E. Ertekin, Lattice mismatch induced ripples and wrinkles in planar graphene/boron nitride superlattices, *J. Appl. Phys.*, 2015, **117**, 234304.
- 40 S. Singh, S. Kim, W. Jeon, K. P. Dhakal, J. Kim and S. Baik, Graphene grain size-dependent synthesis of single-crystalline Sb<sub>2</sub>Te<sub>3</sub> nanoplates and the interfacial thermal transport analysis by Raman thermometry, *Carbon*, 2019, **153**, 164–172.
- 41 K. Lee and J. Ye, Significantly improved thickness uniformity of graphene monolayers grown by chemical vapor deposition by texture and morphology control of the copper foil substrate, *Carbon*, 2016, **100**, 441–449.
- 42 J. C. Meyer, A. K. Geim, M. I. Katsnelson, K. S. Novoselov, T. J. Booth and S. Roth, The structure of suspended graphene sheets, *Nature*, 2007, **446**(7131), 60–63.
- 43 X. Li, Y. Zhu, W. Cai, M. Borysiak, B. Han, D. Chen, R. D. Piner, L. Colombo and R. S. Ruoff, Transfer of large-area graphene films for high-performance transparent conductive electrodes, *Nano Lett.*, 2009, **9**(12), 4359–4363.
- 44 S. Y. Lee, P. Singh and R. L. Mahajan, Role of oxygen functional groups for improved performance of graphene-silicone composites as a thermal interface material, *Carbon*, 2019, **145**, 131–139.
- 45 L. Tapasztó, T. Dumitrică, S. J. Kim, P. Nemes Incze, C. Hwang and L. P. Biró, Breakdown of continuum mechanics for nanometre-wavelength rippling of graphene, *Nat. Phys.*, 2012, **8**(10), 739–742.
- 46 S. Hosseini Hashemi, A. Sepahi Boroujeni and S. Sepahi, Boroujeni, Analytical and molecular dynamics studies on the impact loading of single-layered graphene sheet by fullerene, *Appl. Surf. Sci.*, 2018, **437**, 366–374.
- 47 S. Hosseini Hashemi and A. Sepahi, Boroujeni, Elastic impact response of a nonlocal rectangular plate, *Int. J. Solids Struct.*, 2017, **109**, 93–100.
- 48 A. J. Pak, E. Paek and G. S. Hwang, Tailoring the performance of graphene-based supercapacitors using topological defects: A theoretical assessment, *Carbon*, 2014, **68**, 734–741.
- 49 R. Kumar and A. Parashar, Dislocation assisted crack healing in h-BN nanosheets, *Phys. Chem. Chem. Phys.*, 2017, **19**(32), 21739–21747.
- 50 J. H. Warner, E. R. Margine, M. Mukai, A. W. Robertson, F. Giustino and A. I. Kirkland, Dislocation-driven deformations in graphene, *Science*, 2012, **337**(6091), 209–212.
- 51 Y. Wei, J. Wu, H. Yin, X. Shi, R. Yang and M. Dresselhaus, The nature of strength enhancement and weakening by pentagon-heptagon defects in graphene, *Nat. Mater.*, 2012, **11**(9), 759–763.
- 52 J. Xu, G. Yuan, Q. Zhu, J. Wang, S. Tang and L. Gao, Enhancing the Strength of Graphene by a Denser Grain Boundary, *ACS Nano*, 2018, **12**(5), 4529–4535.
- 53 R. Munoz and C. Gómez, Aleixandre, Review of CVD Synthesis of Graphene, *Chem. Vap. Deposition*, 2013, **19**(10–12), 297–322.
- 54 P. Zheng, X. Zhang, Y. Duan, M. Yan, R. Chapman, Y. Jiang and H. Li, Oxidation of graphene with variable defects: alternately symmetrical escape and self-restructuring of carbon rings, *Nanoscale*, 2020, **12**(18), 10140–10148.
- 55 R. R. Nair, M. Sepioni, I. L. Tsai, O. Lehtinen, J. Keinonen, A. V. Krasheninnikov, T. Thomson, A. K. Geim and I. V. Grigorieva, Spin-half paramagnetism in graphene induced by point defects, *Nat. Phys.*, 2012, **8**(3), 199–202.
- 56 Y. Dong, Y. He, Y. Wang and H. Li, A theoretical study of ripple propagation in defective graphene, *Carbon*, 2014, **68**, 742–747.
- 57 A. Capasso, F. Muñoz Rojas, B. Gupta, N. Motta and E. Placidi, Double grain boundary configurations on graphite surfaces, *Carbon*, 2020, **170**, 630–635.
- 58 J. Zhuang, R. Zhao, J. Dong, T. Yan and F. Ding, Evolution of domains and grain boundaries in graphene: a kinetic Monte Carlo simulation, *Phys. Chem. Chem. Phys.*, 2016, **18**(4), 2932–2939.
- 59 J. Wu and Y. Wei, Grain misorientation and grain-boundary rotation dependent mechanical properties in polycrystalline graphene, *J. Mech. Phys. Solids*, 2013, **61**(6), 1421–1432.
- 60 A. Cresti, J. Carrete, H. Okuno, T. Wang, G. K. H. Madsen, N. Mingo and P. Pochet, Growth, charge and thermal transport of flowered graphene, *Carbon*, 2020, **161**, 259–268.
- 61 E. Cockayne, G. M. Rutter, N. P. Guisinger, J. N. Crain, P. N. First and J. A. Stroscio, Grain boundary loops in graphene, *Phys. Rev. B: Condens. Matter Mater. Phys.*, 2011, **83**(19), 195425.
- 62 S. Plimpton, Fast Parallel Algorithms for Short-Range Molecular-Dynamics, *J. Comput. Phys.*, 1995, **117**(1), 1–19.
- 63 J. Wu, H. Zhao, J. Liu, Z. Zhang, F. Ning and Y. Liu, Nanotube-chirality-controlled tensile characteristics in coiled carbon metastructures, *Carbon*, 2018, **133**, 335–349.
- 64 O. A. Shenderova and D. W. Brenner, Atomistic modeling of the fracture of polycrystalline diamond, *Phys. Rev. B: Condens. Matter Mater. Phys.*, 2000, **61**(6), 3877–3888.
- 65 S. Mukherjee, R. Alicandri and C. V. Singh, Strength of graphene with curvilinear grain boundaries, *Carbon*, 2020, **158**, 808–817.
- 66 S. C. Pradhan and J. K. Phadikar, Nonlocal elasticity theory for vibration of nanoplates, *J. Sound Vib.*, 2009, **325**(1–2), 206–223.
- 67 X. Sun, Z. Wang and Y. Q. Fu, Adsorption and diffusion of sodium on graphene with grain boundaries, *Carbon*, 2017, **116**, 415–421.
- 68 T. Hu, D. Ma, Q. Fang, P. Zhang, X. Liu, R. Wei, Y. Pan, K. Xu and F. Ma, Bismuth mediated defect engineering of epitaxial graphene on SiC(0001), *Carbon*, 2019, **146**, 313–319.

- 69 Y. T. Nam, S. J. Kim, K. M. Kang, W. B. Jung, D. W. Kim and H. T. Jung, Enhanced nanofiltration performance of graphene-based membranes on wrinkled polymer supports, *Carbon*, 2019, **148**, 370–377.
- 70 Y. Zeng, C. L. Lo, S. Zhang, Z. Chen and A. Marconnet, Dynamically tunable thermal transport in polycrystalline graphene by strain engineering, *Carbon*, 2020, **158**, 63–68.
- 71 H. Wu and X. Liu, Tuning electromechanics of dynamic ripple pattern in graphene monolayer, *Carbon*, 2016, **98**, 510–518.
- 72 Y. Z. He, H. Li, P. C. Si, Y. F. Li, H. Q. Yu, X. Q. Zhang, F. Ding, K. M. Liew and X. F. Liu, Dynamic ripples in single layer graphene, *Appl. Phys. Lett.*, 2011, **98**, 063101.